JACS
JOURNAL OF THE AMERICAN CHEMICAL SOCIETY

Article

pubs.acs.org/JACS

Active Sites and Mechanisms for Oxygen Reduction Reaction on Nitrogen-Doped Carbon Alloy Catalysts: Stone–Wales Defect and Curvature Effect

Guo-Liang Chai,*[,†] Zhufeng Hou,[†] Da-Jun Shu,[‡] Takashi Ikeda,[§] and Kiyoyuki Terakura[†,∥,⊥]

[†]Department of Organic and Polymeric Materials, Graduate School of Science and Engineering, Tokyo Institute of Technology, 2-12-1-I6-31 Ookayama, Tokyo 152-8552, Japan

[‡]National Laboratory of Solid State Microstructures and Department of Physics, Nanjing University, Nanjing 210093, China

[§]Condensed Matter Science Unit, Quantum Beam Science Center, Japan Atomic Energy Agency (JAEA), 1-1-1 Kouto, Sayo, Hyogo 679-5148, Japan

[∥]National Institute for Materials Science (NIMS), 1-1 Namiki, Tsukuba, Ibaraki 305-0044, Japan

[⊥]Research Center for Simulation Science, Japan Advanced Institute of Science and Technology (JAIST), 1-1 Asahidai, Nomi, Ishikawa 923-1292, Japan

Supporting Information

ABSTRACT: Carbon alloy catalysts (CACs) are promising oxygen reduction reaction (ORR) catalysts to substitute platinum. However, despite extensive studies on CACs, the reaction sites and mechanisms for ORR are still in controversy. Herein, we present rather general consideration on possible ORR mechanisms for various structures in nitrogen doped CACs based on the first-principles calculations. Our study indicates that only a particular structure of a nitrogen pair doped Stone–Wales defect provides a good active site. The ORR activity of this structure can be tuned by the curvature around the active site, which makes its limiting potential approaching the maximum limiting potential (0.80 V) in the volcano plot for the ORR activity of CACs. The calculated results can be compared with the recent experimental ones of the half-wave potential for CAC systems that range from 0.60 to 0.80 V in the reversible-hydrogen-electrode (RHE) scale.

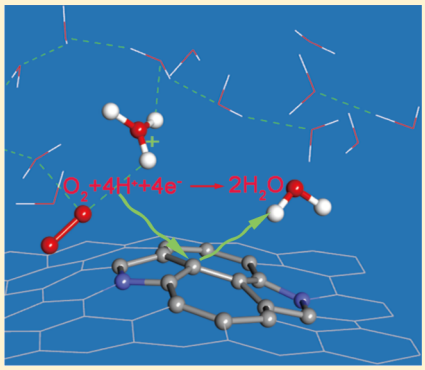

INTRODUCTION

The shortage of energy resources and environmental pollution are two urgent problems in contemporary society. Proton exchange membrane fuel cells (PEMFC) are expected to make important contributions to solve these problems. The efficiency of PEMFC is determined by oxygen reduction reaction (ORR) at the cathode, and up to now the most effective cathode catalysts for the ORR are platinum-based catalysts.[1] However, its large scale commercial applications are hindered by high cost of Pt, and the Pt-based electrode also suffers from low selectivity, poor durability, and CO deactivation.[2,3] Currently, the carbon alloy catalysts (CACs) are the most promising catalysts alternative to Pt-based catalysts because of their good performance for ORR, low cost, rich resource, and free from CO "poisoning",[4,5] although the ORR activity is not yet so high as that of Pt-based catalysts, particularly in acidic conditions. The N-doped CACs are much more intensively studied than the related CACs doped with P, S, and B.[6−8] Generally, the N-containing CACs are synthesized by carbonization of transition-metal macrocyclic compounds together with some carbon sources or N-containing precursors with transition-metal salts.[4,9−11] The basic structural components of CACs are multilayered nanographene (nanographite) including carbon nanotubes (CNTs). Although intensive investigations have been performed on CACs, the active sites and reaction mechanisms are poorly understood and controversial. Whether the ORR activity of N-doped CACs is attributed to pyridinic nitrogen (denoted as p-N), graphitic nitrogen (denoted as g-N), or transition metal elements (such as FeN_x centers) has been a topic of intense debate for a long time.[12−16]

In the present work, we treat only metal-free N-doped carbon catalysts. Even for such limited cases, it is difficult to identify a particular type of p-N or g-N responsible for ORR in experiments because each of the photoemission peaks contains contributions from several different structures with different electronic structures near the Fermi level.[17−19] Theoretical study is therefore needed to supplement the experimental work. In recent years, more and more theoretical studies have been performed on CACs by calculating the ORR potentials.[20−26] To obtain deeper insights into ORR on CACs, we present rather general consideration on possible ORR mechanisms for various structures of nitrogen doped CACs in this paper. The O_2 adsorption barriers for pure Pt surfaces are rather small while

Received: March 15, 2014
Published: September 12, 2014

   dx.doi.org/10.1021/ja502646c | J. Am. Chem. Soc. 2014, 136, 13629−13640

that for CACs is high because graphene and CNTs have strong oxidation resistance. In this paper, both O_2 adsorption barriers and ORR potentials are calculated to search for the ORR active sites. For each structure, we consider not only the conventional standard ORR pathway but also other possible ones such as those involving OH^- and OH radicals. Furthermore, we study the curvature effect on ORR activity by comparing planar graphene sheets with CNTs.

For the conventional standard ORR pathway, a particular structure of N-pair doped Stone–Wales (SW) defect (SW-N3N3′ as shown in Figure 1j) provides an efficient ORR active site with an ORR limiting potential around 0.80 V if the curvature of CNTs is properly tuned. Here, the limiting potential is the highest potential where all of the ORR elementary steps are downhill in free energy. For the reaction pathway involving OH^-, both the SW-N3N3′ structure and the structure with a N-pair doped in the A,B sublattices of a perfect graphene (G-NN^{AB} as shown in Figure 1g) can show an ORR limiting potential around 0.80–0.90 V for some specific CNTs. However, the possibility of such a reaction pathway involving OH^- is dependent on whether the *OOH intermediate exists or not during the ORR process and also affected by other kinetic effects. We also note that the activation barrier for the O_2 adsorption is relatively high (0.64 eV as shown in Table 1) for G-NN^{AB}. The calculated limiting potentials in this paper accord well with the measured half-wave potentials for CACs in experiments in the reversible-hydrogen-electrode (RHE) scale. The experimental results of the half-wave potential for CAC systems range from 0.60 to 0.80 V in the RHE scale.[5,10,27−30]

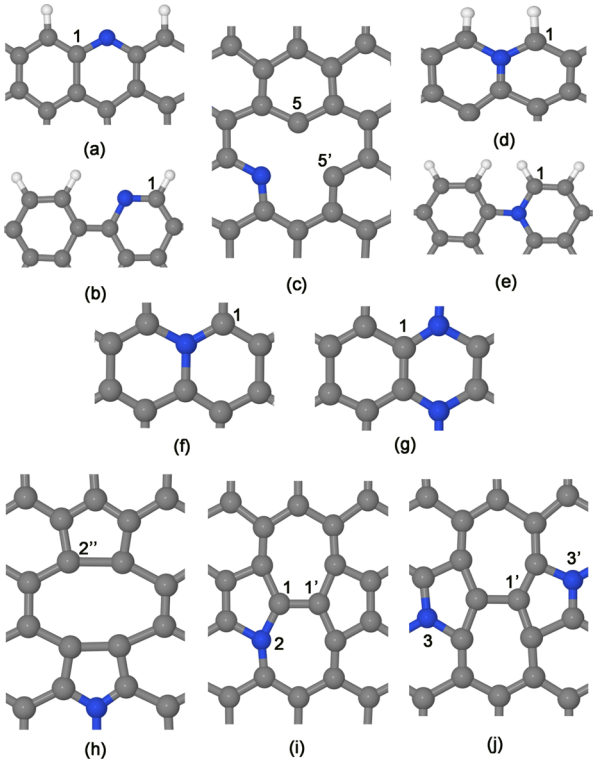

Figure 1. Local atomic structures around N in N-doped graphene. (a) P-N (zigzag), (b) P-N (armchair), (c) MV-N, (d) Edge-1 N (zigzag), (e) Edge-1 N (armchair), (f) G-N, (g) G-NN^{AB}, (h) DV-N, (i) SW-N2, (j) SW-N3N3′. The O_2 approaching C sites are labeled by numbers. Gray, blue, and white balls denote carbon, nitrogen, and hydrogen atoms, respectively.

The remainder of this paper is organized as follows. We describe the models and the computational details in Models and Computational Details. In Results and Discussion, we first discuss the stability of N-doped structures in our models and the free energy profiles of the O_2 adsorption. Then we analyze the standard ORR pathway and also discuss other possible ORR pathways. The conclusion is given in Conclusions.

MODELS AND COMPUTATIONAL DETAILS

Models of Nitrogen Doped CAC Structures. The supercell model with a periodic boundary condition was employed for the calculations of all the nitrogen doped structures. The details of the supercell size will be described later. Figure 1 shows the local atomic structures of different N-doped graphenes, and Table 1 lists some aspects of the structures obtained by our previous paper[31] and also by the present work. The N-doped structures can be classified into three groups according to the type of doped N in CACs: (i) the pyridinic nitrogen (p-N), (ii) pyridinium nitrogen (p-NH), and (iii) graphitic nitrogen (g-N). Note that Table 1 does not explicitly show the cases of p-NH.

As p-N and p-NH can exist only at edges or vacancies, we considered their structures at the zigzag edge, armchair edge, and monovacancy (MV) (Figure 1). Already in one of our previous papers,[31] we showed that the free energy variation for the O_2 adsorption for p-N at the zigzag edge increases monotonically and exceeds 80 kcal/mol (≈ 3.5 eV) as O_2 molecule approaches any edge site. This is also the case for p-NH. We have performed a similar calculation for p-N at the armchair edge and obtained 23 kcal/mol (≈ 1.0 eV) for the O_2 adsorption barrier. This is yet too high for an ORR active site, and the activation barrier is even higher for p-NH. These results imply that p-N and p-NH along zigzag and armchair edges would not contribute to efficient ORR unless some further modification of edges is introduced.[32] The situation is different for p-N at MV. As will be shown later, the activation barrier for the O_2 adsorption is about 12 kcal/mol (≈ 0.50 eV). However, the analysis for subsequent ORR steps suggests that p-N (and p-NH) at MV would not provide an efficient ORR active site either because of too strong binding of the reaction intermediates. So far, we have not succeeded in searching for any single p-N or p-NH structure for efficient ORR. However, we have recently found that a combination of g-N and p-N both along the zigzag edge, for example, has a quite small O_2 adsorption barrier and reasonable ORR performance and that a combination of neighboring p-N and carbonyl will catalyze effectively a two-electron process of reducing O_2 to H_2O_2.[32]

The g-N doped CACs structures have three groups as categorized in Table 1, and some typical examples are shown in Figure 1: (i) g-N at edges, (ii) g-N inside the basal plane, and (iii) g-N around structural point defects. Previously, we proposed that g-N at the edge-1 site of zigzag edge (named edge-1-N(zigzag) and shown in Figure 1d) would be an ORR active site.[31] However, it was shown later that p-NH is much more stable than edge-1-N(zigzag) unless the zigzag edge is mostly dihydrogenated.[17,33] Therefore, the population of edge-1-N(zigzag) will be very small even if they may exist. As these works did not take account of the electrode potential effects, the implication of this site in the context of electrochemical reaction will be discussed later in this work. Note that edge-1-N along the armchair edge causes a large activation barrier of about 38 kcal/mol (≈ 1.6 eV) for the O_2 adsorption.[31]

As to the category of (ii) g-N inside the basal plane, our previous study showed that a single g-N inside the otherwise perfect graphene is not favorable for the O_2 adsorption because of the activation barrier of more than 80 kcal/mol (≈ 3.5 eV).[31] Although the population of this structure is high as suggested by the photoemission analysis, it would not contribute to ORR activity. However, coexistence of two neighboring doped g-N changes the situation. We will study the case of a N–N pair for which two N atoms are located in different sublattices A and B (denoted as NN^{AB}) as shown in Figure 1g. We have also studied NN^{AA} structure in which two N atoms form the shortest pair, with both N atoms occupying the same sublattice. The details of its stability and reactivity will be discussed in a separate paper. Here we only say that

dx.doi.org/10.1021/ja502646c | J. Am. Chem. Soc. 2014, 136, 13629–13640

Table 1. O_2 Adsorption (E_a) and Dissociation Energy (E_d) for Some p-N and g-N Doped CAC Structures, and the Formation Energy (ΔE_f) of N Substitution in Each Structure[a]

	structure	E_a	E_d	ΔE_f	ORR
p-N	C1(P-N)-(zigzag)			0.40	
	C1(P-N)-(armchair)	1.00	0.13	0.26	
	C5(MV-N)	0.53	0.072	−2.15	†
g-N(edge)	C1(edge-1-N)-(zigzag)	0.79[b]	0.74[b]	0.45	†
	C1(edge-1-N)-(armchair)	1.65[b]	0.26[b]	0.66	
g-N(inside)	C1(G-N)			0.78	
	C1(G-NN^{AB})	0.64	0.10	1.64 (0.86)	†
g-N(defect)	C2″(DV-N)			−0.51	
	C1′(SW-N1)			0.19	
	C1′(SW-N2)			0.30	
	C1′(SW-N3)			−0.12	
	C1(SW-N2)	0.80	0.11	0.30	†
	C1′(SW-N3N3′)	0.48	0.082	−0.54	†
	(10, 0)-C1′(SW-N3N3′)	0.54	0.094	−0.017	†
	(9, 0)-C1′(SW-N3N3′)	0.58	0.039	−0.0029	†
	(6, 0)-C1′(SW-N3N3′)	0.29	0.11	−0.21	†

[a]Units are in eV. The ORR pathways will be analyzed for those structures with † mark in the last column. ΔE_f is calculated by the following definition: $\Delta E_f = E_t(mN + host) - E_{tot}(host) - mE_{tot}(N_2) + mE_{tot}(g)$, where $E_{tot}(host)$ and $E_t(mN + host)$ are the total energies of the host before and after nitrogen doping. $E_{tot}(N_2)$ and $E_{tot}(g)$ are the total energies per atom of an N_2 molecule and graphene, respectively. m is the number of N substitutions. For p-N at the ribbon edge, the energy cost for the removal of hydrogen is included in ΔE_f. The number 0.86 in the parentheses of ΔE_f for C1(G-NN^{AB}) corresponds to the formation energy of additional N dopant at the G-N defect (see the text). [b]Reference 31.

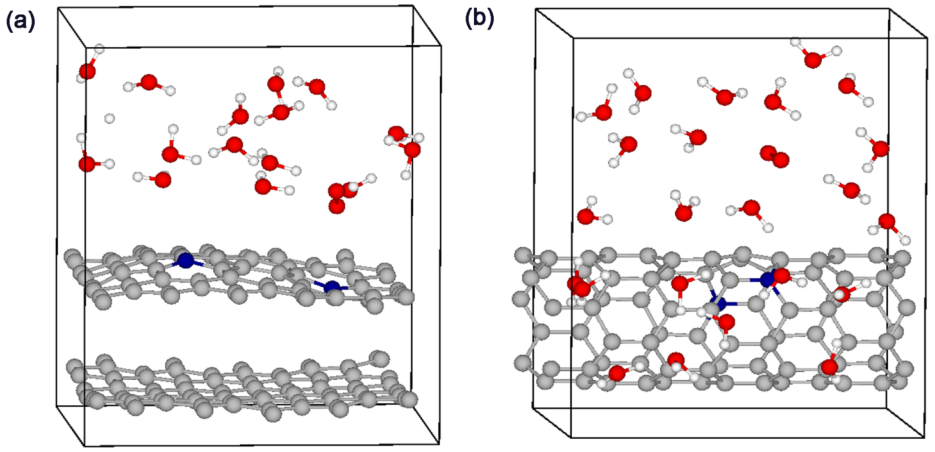

Figure 2. Supercells for the simulation of O_2 molecule adsorption on (a) graphene and (b) (6,0) CNT. The Gray, blue, red, and white balls represent carbon, nitrogen, oxygen, and hydrogen atoms, respectively.

NN^{AB} is more stable than NN^{AA34} and that NN^{AA} does not serve as an active site for four-electron ORR.

For the category of (iii) g-N around structural point defects, we mainly considered divacancy (DV) and Stone−Wales (SW) defect. This is partly motivated by experimental results that the CACs synthesized by precursors containing N-doped five-membered rings can have good performance for ORR,[35,36] and our density functional theory (DFT) calculation[34] suggests that the stable g-N structures at DV and SW defects are actually a N-doped five-membered ring. There is also a DFT calculation which showed that the dissociation barrier of the O_2 adsorption is significantly reduced near N doped at a SW defect.[37] (Note that in most of N doped CACs, the possible active sites are not the doped N but its neighboring carbon atoms.)

Summarizing the above arguments, we deal with the following structures in the present work: (1) p-N and p-NH at MV (denoted as MV-N and MV-NH), (2) p-N at zigzag edge and armchair edge, (3) g-N along the zigzag edge (denoted as edge-1-N(zigzag)), (4) g-N inside the otherwise perfect graphene (denoted as G-N), (5) a pair of g-N for the AB sublattice (denoted as G-NN^{AB}), (6) g-N near DV (denoted as DV-N), (7) g-N near SW defect (denoted as SW-N). Among them, the O_2 adsorption barriers for p-N at the zigzag edge, edge-1-N and G-N were already shown in our previous work.[31] The ORR activity is determined by the bond strength between catalysts surfaces and adsorbed oxygen containing intermediates (*O, *OH, and *OOH).[38−41] The bond strength of these intermediates can be tuned by the details of the local structure including the curvature and N doping. In this paper, the N doped graphene (characterized by sp^2 hybridization) is considered first, and then the carbon nanotubes (CNTs) with different curvature (namely, with different ratios of sp^2 and sp^3 hybridization) are considered to tune the ORR activity.

Computational Details. The Car−Parrinello molecular dynamics simulations were performed to calculate the free energy profiles of the O_2 adsorption by using the CPMD code.[42,43] The Blue Moon ensemble[44] was generated at 300 K by velocity rescaling.[31] The time

dx.doi.org/10.1021/ja502646c | J. Am. Chem. Soc. 2014, 136, 13629−13640

step of 4.0 au (≈ 0.097 fs) was adopted. The distance between the center of an O_2 molecule and the selected carbon site was constrained to compute the free energy profile. For each free energy profile, the total simulation time was about 30 ps. The valence−core interaction was described by Troullier−Martins pseudopotentials (PP) for C, N, and O and von Barth-Car PP for H, respectively.[45,46] The GGA-HCTH exchange-correlation functional was adopted in a spin unrestricted scheme.[47] The use of the HCTH version is very important in the present simulation of an O_2 molecule adsorption because unlike some other versions of GGA, it gives a very reliable binding energy and bond distance of an O_2 molecule.[48] In the adsorption process, an O_2 molecule changes its spin state from triplet (for an isolated molecule) to singlet (adsorbed state), which is discussed in Supporting Information (Figures S2 and S3). The sampling of the Brillouin zone was restricted to the Γ point. The simulation boxes with periodic boundary conditions for the O_2 adsorption are shown in Figure 2a,b. Each simulation box contains a CAC, a certain number of water molecules, and an O_2 molecule. Water molecules were added because the molecularly adsorbed state of O_2 is stabilized by water solvation. The density of water molecules is about half of that of normal liquid water for both cases of graphene and CNTs. The CACs are composed of two layers of graphene sheets, with 60 atoms per layer or carbon nanotubes with the tube length of approximately 12.78 Å as shown in Figure 2a,b. With this choice of the tube length in a supercell, the number of atoms for (6, 0) and (10, 0) CNTs are 72 and 120, respectively.

The total energies of the ORR intermediates were calculated by stationary DFT calculations by employing PWSCF code in Quantum ESPRESSO suite to obtain ORR potentials.[49] The GGA-PBE exchange-correlation functional was adopted.[50] Spin polarization was taken into account if it existed. The kinetic energy cutoffs for the wave function and the charge were set to be 35 and 350 Ry, respectively. For the N doped graphene, an orthorhombic supercell with 60 atoms was used. The lattice parameters parallel to the graphene are about 12.28 and 12.76 Å, and the vacuum region perpendicular to the graphene is about 10.00 Å. For (n, 0) CNTs with n ranging from 6 to 18 (the number of atoms ranging from 72 to 216 correspondingly), the lattice parameter along the tube axis is 12.78 Å. The vacuum region is about 10 Å to mitigate the image−image interaction. The k-point sampling in the Brillouin zone is set to be 5 × 5 × 1 and 1 × 1 × 5 for graphene and CNTs, respectively. The total energies were converted to Gibbs free energies by the simple prescription given by Rossmeisl et al.[51] The details are described in the Supporting Information.

RESULTS AND DISCUSSION

Stability and O_2 Adsorption Barriers for N-Doped CAC Structures. We first calculated the formation energies ΔE_f for different nitrogen doped CAC structures and summarize the results in Table 1. All the formation energies in Table 1 associated with defects correspond to the energy for N doping to the existing defects. Negative (positive) formation energy means that the N doping is exothermic (endothermic). Note that the N_2 gas is used as a reference for the present calculation of ΔE_f. As the N_2 gas is quite stable, most of the calculated ΔE_f are positive. The precursors for nitrogen can be different in experiments, such as N_2, NH_3, and N-containing organic compounds. With some precursor as a reference, ΔE_f may become negative. Therefore, G-N is commonly seen in N-doped graphene despite large ΔE_f in Table 1. Anyway, we can see the relative stability by using the same reference for the formation energy.

We make two more comments on the formation energies in Table 1. First, the formation energy of G-NN^{AB} is largely positive due mostly to the above reason. If we regard G-N as a kind of defect existing already, the formation of G-NN^{AB} is taken to be 0.86 eV, which is larger than ΔE_f for isolated G-N only by 0.08 eV, suggesting that the N−N interaction for G-NN^{AB} is weakly repulsive.[34] Second, among three doping sites at the SW defect, SW-N3 is the most stable one while SW-N1 and SW-N2 are not thermodynamically stable. However, as their energy differences are rather small, we will study all the three structures. As shown in Figure 3a, SW-N3N3′ is the most stable N-doped structure at a SW defect.

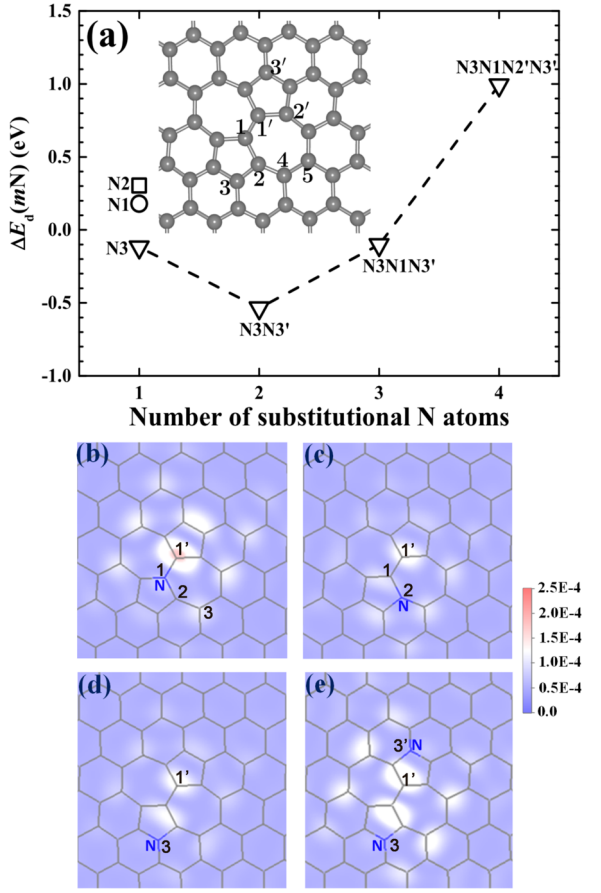

Figure 3. (a) Formation energies of nitrogen substitution at a SW defect in graphene. (b−e) Simulated STM images for different structures of N-doped SW defect in graphene under a bias voltage of −0.2 V and with a sample-tip distance of d = 2 Å. These results are adopted after rearrangement from those in our previous studies.[19,34]

As there are several different sites in each N-doped CAC structure, candidates for an ORR active site which is approached by an O_2 molecule should be selected before the detailed study of the O_2 adsorption barrier. For the structures with doped N along edges and inside the perfect graphene (that is, p-N along zigzag and armchair edges, G-N and G-NN^{AB}), the C sites near the doped N atom which have large density of states (DOS) near the Fermi level[31,33] were selected as the candidates for ORR active sites. The bright sites in the simulated scanning tunneling microscope (STM) image correspond to those sites. Accordingly, the C5 and C2″ sites were selected for MV-N and DV-N.[34] These sites are denoted as C5(MV-N) and C2″(DV), respectively, and the same convention is adopted for other cases. For SW-N structures, the C1′ site (the brightest site) was selected as shown in Figure 3. The criterion for selecting a possible active site was inspired by the frontier molecular orbital theory.[52−54] The DOS near the Fermi level is similar in nature to the highest occupied molecular orbitals (HOMOs) which can donate electrons to an O_2 molecule. To validate this prescription, we test four different sites (C1′, C2, C3, and N1 sites) for SW-N1 structure. The C1′ site has much larger DOS just below the

dx.doi.org/10.1021/ja502646c | J. Am. Chem. Soc. 2014, 136, 13629−13640

Fermi level than other sites. The barrier for an O_2 molecule approaching the C1′ site is much lower than that for other sites as shown in Figure S4 in Supporting Information.

The free energy profiles for the O_2 adsorption to various sites are shown in Figure 4, and the adsorption (E_a) and desorption

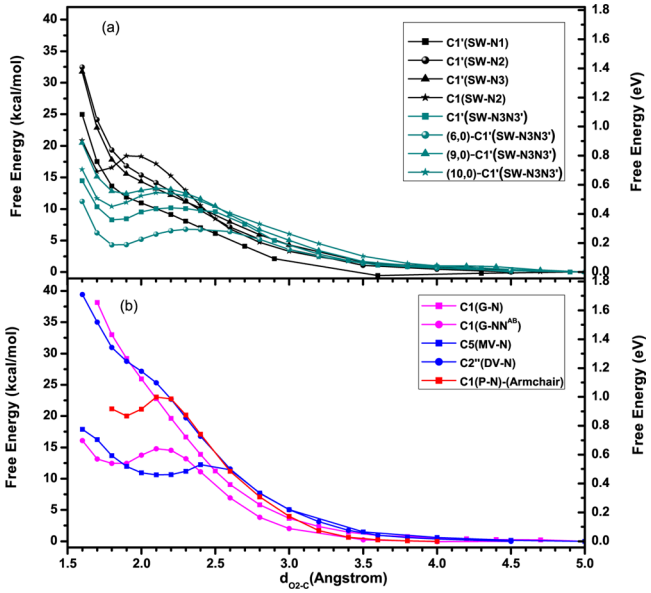

Figure 4. Free energy profiles for O_2 molecule adsorption as a function of the distance between the adsorption site and the center of O_2 molecule for given carbon sites in N-doped graphenes and carbon nanotubes: (a) graphitic N at Stone−Wales defects and (b) graphitic N (in perfect graphene and at divacancy) and pyridinic N (at monovacancy and along armchair edge).

(E_d) barriers for the selected sites (including the results in our previous paper)[31] are summarized in Table 1. Figure 4 shows that there are no stable (metastable) O_2 adsorption at C1′ site for (SW-N1), (SW-N2) and (SW-N3) and also at C1(G-N) and C2″(DV-N) sites. For a single N dopant at SW defect, only C1(SW-N2) site has a metastable O_2 adsorption, although the activation barrier E_a is fairly high (0.80 eV). The adsorbed O_2 molecule takes an end-on structure as shown in Figure S1a in Supporting Information. Note that the C1(SW-N2) site has higher O_2 adsorption free energy than that of C1′(SW-N2) site in the range of $d_{O2-C} > 2.0$ Å in Figure 4a, which reflects the fact that C1 site has lower DOS near the Fermi level than that of C1′ site as suggested by Figure 3c. The metastable O_2 adsorption state is due to cleavage of the N2−C1 bond (see Figure S1 in Supporting Information). The C1(SW-N2) structure will be investigated later in connection to the Sabatier principle in the volcano plot as an example that has strongly bonded ORR intermediates.

In contrast to one N dopant at a SW defect, the structures with two N dopants at a SW defect have metastable O_2 adsorption. The O_2 adsorption barrier for C1′(SW-N3N3′) is about 0.48 eV, and the adsorption structure is also shown in Figure S1 in Supporting Information (also an end-on configuration). The variation of the activation barrier with respect to the CNT curvature is not monotonic. The activation barrier for (6, 0) CNT is reduced to 0.29 eV, while those for (9, 0) and (10, 0) are 0.58 and 0.54 eV, respectively. For the nitrogen pair doped perfect graphene, the O_2 adsorption barrier for C1(G-NN^{AB}) site is about 0.64 eV with a metastable adsorption structure. For the CAC systems studied in this paper, the O_2 adsorption barriers are much higher than desorption barriers as shown in Table 1, which implies that the reaction rate for the O_2 adsorption is much slower than the desorption rate leading to suppression of the ORR rate. However, the O_2 adsorption is accompanied by the proton transfer in the acid condition, which would accelerate to some extent the forward reaction of the O_2 adsorption. Anyway, the overall ORR reaction will be sluggish if the O_2 adsorption barrier is too high. Therefore, only the structures with relatively small O_2 adsorption barrier will be investigated further.

In the following subsections, we will first study the conventional standard ORR pathway and then other possible ORR pathways for the cases which have stable (metastable) O_2 adsorption states and relatively low O_2 adsorption barriers ($E_a \leq$ 0.80 eV) as shown in Figure 4. The choice of the critical value of 0.8 eV for E_a has no definite meaning but may be reasonable from the above arguments. The sites with a † sign in the last column of Table 1, that is, C1(edge-1-N)-(zigzag), C5(MV-N), C1-(NN^{AB}), C1(SW-N2), and C1′(SW-N3N3′), are chosen accordingly. However, we will point out below that the C−OH bond is too strong at C1(edge-1-N)-(zigzag) and C5(MV-N) sites for proper ORR activity. Thus, only C1(NN^{AB}), C1(SW-N2), and C1′(SW-N3N3′) sites will be investigated systemically from the viewpoint of the curvature effect by using CNTs with different diameters.

Standard Four-Electron ORR Pathway for CACs. The CACs are different from Pt-based catalysts. In all the cases investigated so far for CACs, the adsorbed O_2 takes an end-on configuration and, moreover, unlike Pt-based catalysts, the *OOH intermediate does not decompose to *O + *OH. We therefore call the four-electron associative reaction pathway of eq 1 the standard ORR pathway for CACs:

$$\begin{aligned} O_{2(g)} &\xrightarrow[H^+ + e^-]{\Delta G_1^s} {}^*OOH \\ &\xrightarrow[H^+ + e^-]{\Delta G_2^s} {}^*O + H_2O_{(l)} \\ &\xrightarrow[H^+ + e^-]{\Delta G_3^s} {}^*OH + H_2O_{(l)} \\ &\xrightarrow[H^+ + e^-]{\Delta G_4^s} 2H_2O_{(l)} \end{aligned} \quad (1)$$

The ΔG_i^s (i = 1−4) is the reaction Gibbs free energy for each elementary step. The superscript "s" stands for the standard ORR pathway and will be used only when necessary for the further discussion. In most cases, we neglect it and use ΔG_i for simplicity. In each electrochemical step, one electron transfer is assumed to be coupled with one proton transfer. Here, we assume that the concentration of proton corresponds to the standard condition (pH = 0) and that the electrode potential is equal to the standard hydrogen electrode (SHE) potential for the calculation of ΔG_i. For the electrode potential U with respect to SHE, $\Delta G_i(U) = \Delta G_i + eU$. The limiting potential for each catalytic site is defined as

$$U_L = \mathrm{Min}_i[-\Delta G_i]/ne \quad (2)$$

where n is the number of electrons transferred for each elementary step (here n = 1 for one electron transfer step) and e is the elementary charge. The ΔG_i is in units of eV. The meaning of the right-hand side of the above equation is to select the smallest $[-\Delta G_i]$ among the ORR elementary steps. The limiting potential is the highest potential where all of the ORR elementary steps are downhill in free energy, which can be

dx.doi.org/10.1021/ja502646c | J. Am. Chem. Soc. 2014, 136, 13629−13640

compared with the half-wave potential measured in experiments.[55] In the idealistic situation where U_L of the PEMFC is 1.23 V (neglecting all losses), ΔG_i for each electrochemical step i should be 1.23 eV, and the nonelectrochemical steps such as O_2 adsorption and *OOH decomposition should not produce any free energy changes as discussed by Anderson.[39,56] If any imbalance may exist in the allocation of the given total Gibbs free energy difference (4.92 eV) among the four steps, U_L is determined by the potential-determining step with the smallest $(-\Delta G_i/ne)$.

An efficient and practical method for screening the ORR catalysts has been established by Nørskov et al.[38,41] The reaction Gibbs free energies ΔG_i (i = 1−4) are expressed in terms of the Gibbs free energy changes associated with adsorption of *O (ΔG_{*O}), *OH (ΔG_{*OH}), and *OOH (ΔG_{*OOH}) intermediates as described in the Supporting Information. In the process of estimating ΔG_i, the adsorption energies of O_2 and H_2O on CACs are not taken into account. The neglect of H_2O adsorption energy is reasonable because CAC surfaces are generally hydrophobic. On the other hand, as Figure 4 shows, the metastable O_2 adsorbed state is higher in energy than the initial state with the O_2 separated far from the substrate. Although this aspect may cause some ambiguity in the estimation of ΔG_i, its main effect will be reflected in kinetics as explained below. First, the lifetime of the metastable O_2 adsorbed state on CACs is rather short due to the small desorption barrier as discussed already, and second, the O_2 adsorbed state (*OO) would quickly be converted to *OOH by an electron and proton transfer in the acidic solution. Therefore, the energy of metastable O_2 adsorbed state may not be well-defined, and the reaction rate would be sluggish due to the repulsion between O_2 and CAC surface sites. With such assumptions, the adsorption energies for the above three ORR intermediates can be readily calculated by using the density functional method and converted to adsorption Gibbs free energies by taking account of the entropy, zero-point energy and solvation energy corrections.[57] This allows us to do stationary total energy calculations without including water molecules. Further simplification comes in through the empirical finding of the linear relationships among ΔG_{*O}, ΔG_{*OH}, and ΔG_{*OOH} as shown below.[38,40]

In the present work, these three quantities are calculated for C1′(SW-N3N3′), C1(SW-N2), and C1(G-NN^{AB}) sites for both graphenes and CNTs (see Supporting Information for details of the calculation), and the results are shown in Figure 5. The results of C1(G-N) site are also included for comparison. On the other hand, we find that the C−OH bond is too strong for ORR at C1(edge-1-N)-(zigzag), C5(MV-N), and C5(MV-NH) sites as suggested by the calculated ΔG_{*OH} values of 0.50, 0.34, and −0.60 eV, respectively, because these values are far away from the optimum ΔG_{*OH} value (0.80 eV) as shown below to give a large U_L. As these C−OH bonds will be even stronger by introducing curvature, we do not study the ORR process further for these sites. In Figure 5, solid lines denote the following linear relations:

$$\Delta G_{*O} = 2\Delta G_{*OH} + a \quad (a = 0.30) \tag{3}$$

$$\Delta G_{*OOH} = \Delta G_{*OH} + b \quad (b = 3.33) \tag{4}$$

The "b" value in eq 4 is reliable because of the well-fitted linear relationship between ΔG_{*OOH} and ΔG_{*OH}, which means that the difference between ΔG_{*OOH} and ΔG_{*OH} is constant, being about 3.33 eV for all the possible catalytic sites in N-doped CACs. This constant separation is also observed for metal and metal oxide catalysts, and the constant "b" value is always in the range of 3.0−3.4 eV.[51,58] Compared with the "b" value, the "a"' value has significant uncertainty because the relation of eq 3 is a rough approximation as shown in Figure 5. Fortunately, the potential-determining step for CACs is mostly determined by the "b" value for the standard ORR pathway as will be shown later. Here we make a brief comment on the nonsystematic behavior and the significant scattering of ΔG_{*O} data for C1(G-NN^{AB}) (red circles in Figure 5) as a function of n of (n, 0) CNT. It is caused by the fact that the adsorbed O takes an epoxy-like configuration for n = 6 and 8 and a ketone type for other cases. The adsorption Gibbs free energy discussed here is relative adsorption Gibbs free energy (RAGFE) with the H_2 and H_2O as references and does not give true adsorption bond strength of intermediates. On the other hand, the absolute adsorption Gibbs free energies (AAGFE) for intermediates can reflect the real adsorption bond strength.[39,56] In the present work, we did not calculate the AAGFEs directly by the electronic structure calculations but obtained them from RAGFE. The reason for this and the details of the relation between AAGFE and RAGFE are given in the Supporting Information. We denote AAGFE by adding the superscript "A", namely, ΔG^A_{*O}, ΔG^A_{*OH}, and ΔG^A_{*OOH}, and they are shown in Figure 6. The relations given by eqs 3 and 4 hold also for ΔG^A_{*O}, ΔG^A_{*OH}, and ΔG^A_{*OOH}, with different values for a and b. For AAGFEs, these parameters expressed as a^A and b^A take 0.79 and 1.00 eV, respectively. We note that the AAGFE of *OOH is smaller than that of *OH by 1.00 eV and that this energy difference is physically meaningful.

Each reaction site has a set of [ΔG_{*O}, ΔG_{*OH}, and ΔG_{*OOH}], which determines ΔG_i (i = ∼4) for the reaction site (see eqs S8,

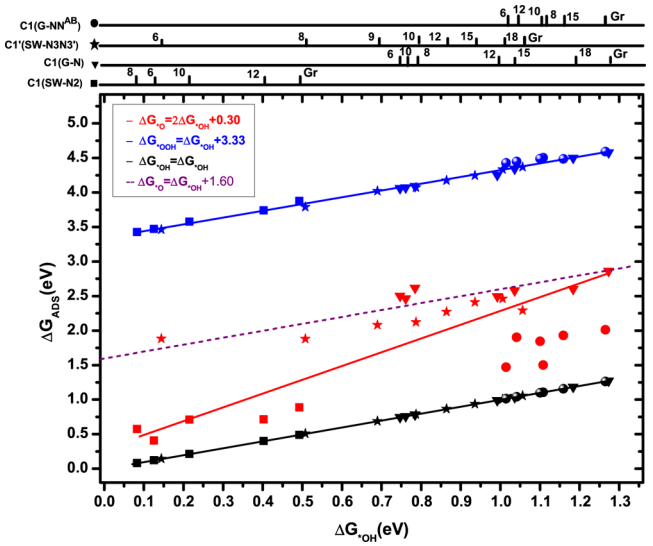

Figure 5. Adsorption Gibbs free energies ΔG_{ADS} of ORR intermediates vs the adsorption Gibbs free energy of *OH intermediate, ΔG_{*OH}. ΔG_{ADS} represents ΔG_{*O}, ΔG_{*OH}, and ΔG_{*OOH}. The symbols for different configurations are shown at the top: square for C1(SW-N2), triangle for C1(G-N), star for C1′(SW-N3N3′), and circle for C1(G-NN^{AB}). The solid red and blue lines correspond to eqs 3 and 4, while the solid black line denotes ΔG_{*OH} itself. It is clear that the difference between ΔG_{*OOH} and ΔG_{*OH} is constant. These lines are fitted by employing linear regression model with the slopes fixed to be 1.0 and 2.0 for ΔG_{*OOH} and ΔG_{*O}, respectively. The adjusted coefficient of determinations R^2 are 0.37 and 0.99 for eqs 3 and 4 respectively. The position of the bar with descriptor "n" for (n, 0) CNT, or Gr for graphene along horizontal lines at the top measures the corresponding values of ΔG_{*OH} for each specific site. The broken purple line shows eq 10 when the equality holds.

dx.doi.org/10.1021/ja502646c | J. Am. Chem. Soc. 2014, 136, 13629−13640

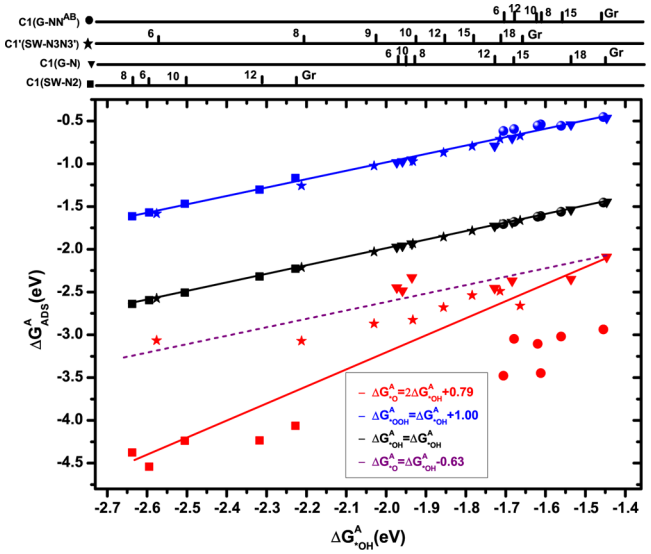

Figure 6. Absolute adsorption Gibbs free energies for ORR intermediates ΔG^{A}_{ADS} vs the absolute adsorption Gibbs free energy of *OH intermediate, ΔG^{A}_{*OH}. ΔG^{A}_{ADS} represents ΔG^{A}_{*O}, ΔG^{A}_{*OH}, and ΔG^{A}_{*OOH}. The values in this figure are converted from Figure 5 as described in the Supporting Information. In this representation, the adsorption energy difference of 1.00 eV between *OOH and *OH is physically meaningful. The position of the bar with descriptor "n" for (n, 0) CNT, or Gr for graphene along horizontal lines at the top measures the corresponding values of ΔG_{*OH} for each specific site. The broken purple line shows eq 10 when the equality holds.

S10, S12, and S14 in the Supporting Information). The calculated results of ΔG_i are shown by circles, stars, and squares in Figure 7. If we use the linear relationships of eqs 3 and 4, the ΔG_i ($i = \sim 4$) can be expressed as functions of ΔG_{*OH} as shown in

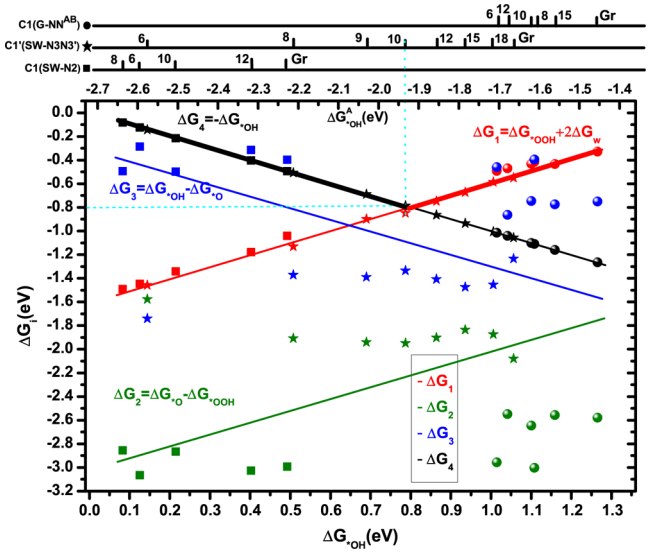

Figure 7. Reaction Gibbs free energies, ΔG_i, for ORR steps. The bottom axis is on the scale of Nørskov's method, and the upper axis is on the scale of the absolute adsorption Gibbs free energy. The lines are fitted by linear relationships of eqs 3 and 4. The limiting potential is determined by the step with the smallest Gibbs free energy decrease for each site and corresponds to the bold black and red lines, which form an inverted volcano plot for ORR. The position of the bar with descriptor "n" for (n, 0) CNT, or Gr for graphene along horizontal lines at the top measures the corresponding values of ΔG_{*OH} for each specific site.

Supporting Information eqs S15−S18. These functions are four straight lines, with ΔG_{*OH} as a descriptor as shown in Figure 7. As the limiting potential for each site is determined by the lines of ΔG_1 or ΔG_4, the ORR active region is the upper region of the bold black and red lines in Figure 7, which form an inverted volcano plot for ORR. The optimum limiting potential of eq 2 is determined by the point of intersection of the lines for ΔG_1 and ΔG_4, which is (2.46−0.5 × b) V = 0.80 V, with the optimum ΔG_{*OH} being 0.80 eV. The calculated limiting potential can be compared with the experimental half-wave potential whose recent results for CAC systems range from 0.60 to 0.80 V in the RHE scale.[5,10,27−30] Note that the limiting potential and the optimum ΔG_{*OH} only depend on the "b" value, and the "b" value determined by eq 4 is reliable as discussed before. In Figure 7, not only ΔG_{*OH} calculated by Nørskov's method is plotted along the lower horizontal axis but also the AAGFE ΔG^{A}_{*OH} is plotted along the upper horizontal axis. Along the three horizontal lines at the top of Figure 7, short bars with "n" indicate the position of ΔG_{*OH} and ΔG^{A}_{*OH} for (n, 0) CNT or for Gr denoting graphene at the reaction sites for each category of C1′(SW-N3N3′), C1(SW-N2), and C1(G-NN^{AB}).

This diagram shows that the data for C1(SW-N2) site are located in the left side of the active region (the ORR intermediates being strongly bonded to CACs), while those of C1(G-NN^{AB}) site are located in the opposite region (the ORR intermediates being weakly bonded to CACs). Thus, both of the two sites have low activity within the standard ORR pathway. Only C1′(SW-N3N3′) sites occupy a broad region covering the optimum condition for ORR. Therefore, we conclude that C1′(SW-N3N3′) sites with proper curvature is a promising ORR active site and even some errors caused by some approximations would not change the conclusion.

The volcano plot is a demonstration of the Sabatier principle that a good catalyst binds the key intermediates neither too weakly nor too strongly[59] and the curvature of CNT controls the bond strength. Supporting Information Figure S6 shows the curvature dependence of ΔG^{A}_{*OH}. We can see that the bond strength increases with the increase of curvature. The origin of the curvature effect mainly comes from the change of hybridization in the carbon electronic structure. For the graphene with zero curvature, the sp^2 hybridization before adsorption is converted partly to the sp^3 hybridization after adsorption of intermediates. The well conjugated structure of graphene impedes the sp^2 to sp^3 conversion. However, the use of CNTs makes it possible to control the degree of the sp^3 hybridization. The relation between sp^2 and sp^3 configurations is semiquantitatively analyzed by the bond angle dependence around the reaction site.[60,61] Further discussion about this analysis is given in the Supporting Information, and the results are shown in Figures S6 and S7. Figure 8 shows the CNT-curvature dependence of the U_L for the structures studied in this work. For the C1′(SW-N3N3′) site, CNTs with some specific curvatures, such as (9, 0), (10, 0), and (12, 0) CNTs, are close to the optimum situation, producing the maximum limiting potential of about 0.80 V. This value is comparable to that of Pt(111) surface (0.79 V).[62]

As a SW defect may serve as a good active site, here we discuss the possibility for the formation of a SW defect. Note that the formation energies in Table 1 associated with defects correspond to N doping energy to the existing defects. The formation energy of pure MV, DV, and SW defects in graphene were calculated to be 7.54, 7.44, and 4.88 eV, respectively.[34] The SW defects in CNTs can have different directions, that is, parallel or oblique to

dx.doi.org/10.1021/ja502646c | J. Am. Chem. Soc. 2014, 136, 13629−13640

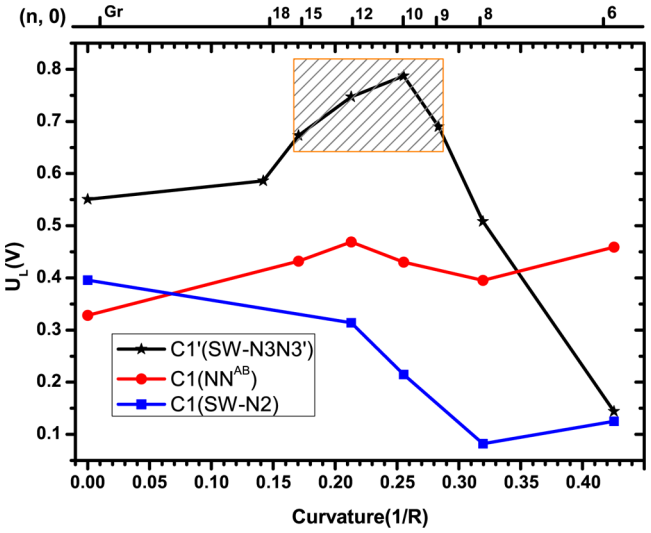

Figure 8. Limiting potential versus the curvature ($1/R$ with R the radius) of CNTs. The limiting potential is evaluated by eq 2 for each site. The position of the bar with descriptor "n" for (n, 0) CNT, or Gr for graphene along the horizontal line at the top measures the corresponding values of $1/R$ for each specific site.

the tube axis. The SW defect parallel to the tube axis is more stable than that oblique to the tube axis.[63] In this paper, all the investigated SW defects in CNTs are parallel to the tube axis. The calculated formation energies range from 2.30 to 3.93 eV for the parallel SW defects in CNTs from (7, 0) to (18, 0) CNTs as shown in a previous study by others,[63] which is consistent with the experimental finding that large diameter CNTs have fewer SW defects than small diameter CNTs.[64] The formation energy of a SW defect in CNTs decreases significantly compared with that in graphene. This is mainly because the SW defect can release the stress in CNTs. Moreover, the SW-N3N3′ structure is the most stable structure for N doped SW defect as shown in Figure 3. Thus, the population of N-doped SW defect should be increased by using small diameter CNTs, which may provide a good method to improve the activity of ORR on CACs.

Other Possible Reaction Pathways. Some other possible ORR pathways may be conceived in addition to the standard reaction pathway as discussed above. Figure 9 is a summary of the possible ORR mechanisms. In Figure 9a, the intermediate

(a) ORR pathways with stable *OOH intermediate

$$O_{2(g)} + * \longrightarrow *OO \xrightarrow{H^+ + e^-} *OOH \begin{cases} \xrightarrow[\text{standard model}]{(1)\ H^+ + e^-} *O + H_2O_{(l)} \\ \xrightarrow{(2)\ H^+ + e^-} * + H_2O_{2(aq)} \end{cases}$$

(b) ORR pathways with transient *OOH

$$O_{2(g)} + * \longrightarrow *OO \xrightarrow{H^+ + e^-} (*OOH) \begin{cases} \xrightarrow{(3)} *O + OH_{(aq)} \longrightarrow *O + *OH \xrightarrow{H^+ + e^-} *O + H_2O_{(l)} \\ \xrightarrow{(4)\ e^-} *O + OH^-_{(aq)} \xrightarrow{H^+} *O + H_2O_{(l)} \\ \xrightarrow{(5)\ e^-} * + OOH^-_{(aq)} \xrightarrow{H^+} * + H_2O_{2(aq)} \end{cases}$$

(c) Reduction process of *O

$$*O \xrightarrow{H^+ + e^-} *OH \xrightarrow{H^+ + e^-} *H_2O_{(l)}$$

Figure 9. Some possible ORR pathways in acidic solution. The details about the possibility of these reaction pathways and lifetimes of OH^- and OOH^- intermediates in acidic solution are discussed in the Supporting Information.

*OOH is assumed to be stable unless it is attacked by a proton coupled with an electron transfer. The reaction pathway 1 is the standard four-electron reaction pathway that is already discussed in the preceding subsection. On the other hand, Figure 9b shows some possible reaction pathways in which *OOH is not a stable intermediate. Figure 9c shows the reduction process of *O intermediate that is produced by the last step of reaction pathways 1, 3, and 4 to complete the overall reactions.

We have found in our first-principles molecular dynamics (FPMD) simulations that the *OOH intermediate is often unstable and does not exist in some cases. Our observation was also supported by a similar calculation[65] in which the O−O bond of *OOH was cleaved only after 600 fs. These results motivated us to consider the reaction pathways in Figure 9b. The meaning of *OOH in parentheses is that even if *OOH is formed, its lifetime is too short for the thermal equilibrium to be achieved even without being attacked by a proton and an electron. Therefore, we regard *OOH as a transient state rather than a stable reaction intermediate. Note that an electron transfer is not simultaneously coupled with a proton transfer in the reaction pathways 4 and 5.[66] Therefore, the electrochemical step from *OO to *O + $OH^-_{(aq)}$ and also the one from *OO to * + $OOH^-_{(aq)}$ are the two-electron and one-proton transfer step, which was also suggested by an experimental findings for photocatalysts.[67] The reaction pathways 4 and 5 involve $OH^-_{(aq)}$ or $OOH^-_{(aq)}$ intermediates. The details about the possibility of these reaction pathways and lifetimes of $OH^-_{(aq)}$ and $OOH^-_{(aq)}$ intermediates in acidic solution are discussed in the Supporting Information. Below we discuss which reaction pathway among those shown in Figure 9 is the probable one depending on the bond strength of ORR intermediates.

First, we discuss the condition under which *OOH is decomposed into *O and free radical OH or equivalently the reaction pathway 3 is more favored than the reaction pathway 1. Such a condition is given by

$$G(\text{sub-O}) + G(OH_{(aq)}) < G(\text{sub-OOH}) \tag{5}$$

where G(sub-O) and G(sub-OOH) are free energies of the substrate with the adducts *O and *OOH, respectively, and $G(OH_{(aq)})$ is the free energy of OH radical in the aqueous water. Then, we obtain the following equation for CACs by using the experimental data for the chemical potential of OH radical in aqueous water (the derivation is given in Supporting Information):

$$\Delta G_{*O} < \Delta G_{*OH} + 0.60 \quad (\text{in eV}) \tag{6}$$

From Figure 5, we see that there are seven sites that satisfy eq 6 and their ΔG_{*OH} are either in the range of less than 0.60 eV or around 1.0 eV.

The free OH radical may be adsorbed at another reaction site as *OH, and then the resulting *O and *OH would be further reduced to water separately. The reaction pathway 3 is similar to the case of dissociative oxygen adsorption. However, in contrast to Pt catalyst, oxygen molecule is generally adsorbed to CAC in an end-on configuration so that the dissociative oxygen adsorption is impossible. Anyway, in the subsequent reduction process of *O, we can show (see Supporting Information for details) that the free energy change for the process of converting *O to *OH has to be larger than −0.60 eV as long as eq 6 is satisfied. Therefore, for the reduction step of *O, the largest U_L is only 0.60 V. On the other hand, the reduction process of another adduct *OH can produce higher potential. Nevertheless, as only

dx.doi.org/10.1021/ja502646c | J. Am. Chem. Soc. 2014, 136, 13629−13640

two electrons (rather than four) can contribute to this output potential, the electric current is also only half of the usual four-electron reaction pathways. These considerations suggest that the reaction pathway 3 would occur only under some limited condition and that even if the process is realized, it would not be favorable for optimal ORR. Because of strong binding of *O, CAC would be oxidized.

Second, we compare the relative stability of the intermediates between the reaction pathways 4 and 5. We use the thermodynamic data of the standard formation free energies for $OOH^-_{(aq)}$ and $OH^-_{(aq)}$, $\Delta_f G(OOH^-_{(aq)}) = -67.30$ kJ/mol ≈ -0.70 eV, and $\Delta_f G(OH^-_{(aq)}) = -157.24$ kJ/mol ≈ -1.63 eV.[68] Then we obtain the following relation as the difference in the free energy $\Delta G_{(4),(5)}$ of intermediates between the two reaction pathways (4) and (5) (see Supporting Information):

$$\Delta G_{(4),(5)} = G_{(5)} - G_{(4)} = 3.39 - \Delta G_{*O} \quad (\text{in eV}) \tag{7}$$

This quantity is positive for almost all catalytic sites studied in this work, which means that the reaction pathway 5 is less probable than the reaction pathway 4 as long as the equilibrium free energy is concerned. However, for C1(G-NN^{AB}) site, the relatively large ΔG_{*OOH} as shown in Figure 5 implies that the C−OOH bond is weak and that the process 5 may be kinetically possible as is sometimes observed in our FPMD simulations.

Third, we discuss the condition under which the reaction pathway 4 is more favorable than the standard reaction pathway 1 from the equilibrium free energy viewpoint. The condition to realize this situation is given by

$$G(\text{sub-O}) + G(OH^-_{(aq)}) < G(\text{sub-OOH}) - eU \tag{8}$$

where e is the elementary charge and U is the electrode potential. With the use of thermodynamic data of the standard formation free energy of $OH^-_{(aq)}$ of −1.63 eV and eq 4, eq 8 can be converted to (see Supporting Information)

$$\Delta G_{*O} < \Delta G_{*OH} + 2.50 - eU \quad (\text{in eV}) \tag{9}$$

Noting that the largest U achieved is about 0.90 V, and eq 9 is reduced to

$$\Delta G_{*O} < \Delta G_{*OH} + 1.60 \quad (\text{in eV}) \tag{10}$$

If we further use eq 3, eq 10 is simply expressed as

$$\Delta G_{*O} < 1.40 \quad (\text{in eV}) \tag{11}$$

Equation 11 is satisfied for almost all the cases we have studied, which means that the reaction pathway 4 is more thermodynamically favorable than the standard reaction pathway 1 . However, eq 3 is a crude approximation and a few cases do not satisfy eq 10. In Figures5 and 6, the broken purple line shows eq 10 when equality holds. For C1(SW-N2) site, eq 10 always holds and only *O and OH^- intermediates are found in the FPMD simulations, which suggests that the reaction pathway 4 is rather favorable for this site. Clearly, the cases of C1′(SW-N3N3′) site are close to this line and (6, 0)-C1′(SW-N3N3′) does not satisfy eq 10. Moreover, the presence of the activation barrier for *OOH cleavage may stabilize *OOH for a while even if eq 10 is satisfied. This is in fact correlated with our observation that *OOH is relatively stable in the FPMD simulation for SW-N3N3′ site in graphene.[69] Furthermore, the reaction pathway 5 may be more favorable than the reaction pathway 4 for C1(G-NN^{AB}) site again because of the kinetic reasons. Keeping the existence of some exceptional cases in mind, we analyze the ORR steps according to the reaction pathway 4 in the next subsection. For the steps that involve OH^- or OOH^- intermediates, the neutralization energies of these alkalic intermediates in acidic solution should be responsible for the energy loss that will not contribute to the electron transfer steps. The energy loss by nonelectron transfer step on the electrode would limit the maximum limiting potential that can be obtained in PEMFC, as discussed by Anderson et al.[39,56]

Before closing this subsection, we make a brief comment on the formation of H_2O_2 referring to the reaction pathway 2 in Figure 9. Indeed, this reaction pathway was argued by Nørskov et al. for metal surfaces.[55] However, we found that the possibility of H_2O_2 formation through the O_2 adsorption is quite low due to the hydrophobicity of CACs. The reaction pathway of H_2O_2 formation without the O_2 adsorption is possible, which we will discuss in a separate paper.

Details of Reaction Pathway 4. As the reaction pathway (4) is thermodynamically rather favorable, we discuss more details about it in this subsection. We show in eq 12 the reaction pathway (4) by removing the transient state *OOH from Figure 9b. The definition of the reaction free energy of each elementary step is also given in eq 12.

$$\begin{aligned} O_{2(g)} &\xrightarrow[(H^+ + e^-) + e^-]{\Delta G_1^t} *O + OH^-_{(aq)} \\ &\xrightarrow[H^+]{\Delta G_2^t} *O + H_2O_{(l)} \\ &\xrightarrow[H^+ + e^-]{\Delta G_3^s} *OH + H_2O_{(l)} \\ &\xrightarrow[H^+ + e^-]{\Delta G_4^s} 2H_2O_{(l)} \end{aligned} \tag{12}$$

where the superscript "s" of ΔG_i^s stands for one-electron transfer step existing in the standard ORR pathway and the superscript "t" of ΔG_i^t for the steps related with two successive electron transfers. As described in detail in the Supporting Information, we have an expression for the reaction free energy of the first reaction step as

$$\Delta G_1^t(U) = \Delta G_{*O} - 4.09 + 2eU \tag{13}$$

where we explicitly include the electrode potential U to show that the step involves two electrons.[66] On the other hand, the second step in eq 12 is not an electrochemical step and is simply given by

$$\Delta G_2^t = G(H_2O) - G(OH^-_{(aq)}) - G(H^+_{(aq)}) = -0.83 \tag{14}$$

in eV. The value of −0.83 eV is the experimental one for the free energy variation of neutralization under the standard condition. The total Gibbs free energy available to the electrochemical ORR steps (4.92 eV) is reduced by the nonelectrochemical energy loss of 0.83 eV.[39,56] The rest of 4.09 eV is distributed among the three electrochemical reaction steps. The Gibbs free energy variation diagram for the reaction pathway 4, which corresponds to Figure 7 for the reaction pathway 1, is shown in Figure 10. If we use eq 3, the optimum U_L is given by $(1.02-0.25a)$ V = 0.95 V (a = 0.30 for CAC). Note, however, that the optimum U_L is now directly affected by ΔG_{*O} for which eq 3 is not so accurate. Therefore, as Figure 10 shows, the above analytical results are only approximate but there are several cases for which the U_L ranges between 0.80 and 0.90 V. In Figure 11, we summarize the CNT-curvature dependence of the U_L for some nitrogen doped structures. In contrast to Figure 8, not only C1′(SW-N3N3′) but also C1(G-NN^{AB}) are candidates for desirable catalytic sites with a wide range of CNT curvature. However, two aspects need to be

dx.doi.org/10.1021/ja502646c | J. Am. Chem. Soc. 2014, 136, 13629−13640

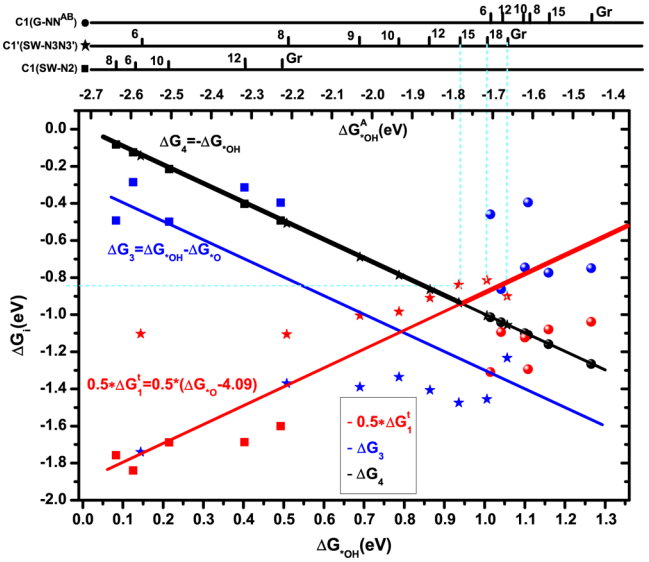

Figure 10. Reaction Gibbs free energies, ΔG_i, for ORR steps of the reaction pathway 4. The bottom axis is on the scale of Nørskov's method, and the upper axis is on the scale of the absolute adsorption Gibbs free energy. The position of the bar with descriptor "n" for $(n, 0)$ CNT, or Gr for graphene along horizontal lines at the top measures the corresponding values of ΔG_{*OH} for each specific site.

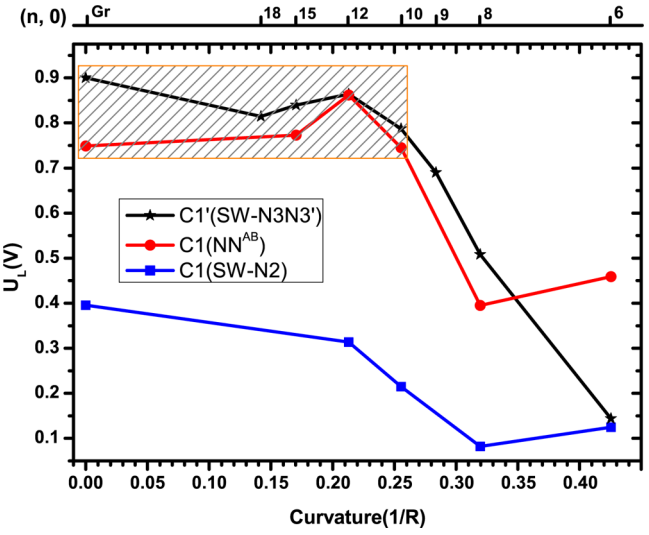

Figure 11. Limiting potential versus the curvature $(1/R$ with R the radius) of CNTs for the process 4. The limiting potential is evaluated by eq 2 for each site. The position of the bar with descriptor "n" for $(n, 0)$ CNT, or Gr for graphene along the horizontal line at the top measures the corresponding values of $1/R$ for each specific site.

taken into account. First, as stated in the preceding subsection, *OOH is relatively stable for SW-N3N3′, which may reduce the possibility of the reaction pathway 4. Second, the ΔG_{*OOH} of C1(G-NN^{AB}) site may favor the reaction pathway 5 by kinetic reasons. This site also has a relatively large activation barrier for the O_2 adsorption.

CONCLUSIONS

Different structures of nitrogen doped CACs are considered to search the ORR active sites. Two aspects were studied for ORR activity. First the free energy barrier for the O_2 adsorption was calculated by the first-principles molecular dynamics simulations, and second the reaction Gibbs free energy for each electrochemical elementary step was calculated by using the prescription given by Nørskov et al.[38,41] In this respect, we discussed some possible ORR pathways. Detailed analyses were made not only for the standard reaction pathway but also for a reaction pathway in which *OO is converted to *O + $OH^-_{(aq)}$ via two successive electron transfer steps. With the results of these calculations, we found that C1′(SW-N3N3′) site has good performance for the standard four-electron ORR. The ORR activity of this site can be tuned by using carbon nanotube to introduce the curvature effect. Our results show that C1′(SW-N3N3′) site with some specific curvatures, such as (9, 0), (10, 0), and (12, 0) CNTs, approaches the maximum ORR activity (0.80 V) in the activity volcano plot for the standard reaction pathway (comparable to that of Pt catalyst). For another reaction pathway involving $OH^-_{(aq)}$ formation, the limiting potential U_L ranging between 0.80 and 0.90 V can be obtained both for C1′(SW-N3N3′) and C1(G-NN^{AB}) sites. Note, however, that the probability of this reaction pathway for C1′(SW-N3N3′) site may be reduced by competing with the reaction pathway 1 and the probability of this reaction pathway for C1(G-NN^{AB}) site is reduced by competing with the reaction pathway 5. Although the two successive electron transfer reaction pathway is thermodynamically rather favorable, the reaction pathway is also affected by the kinetics. The possibility of the two-successive-electron-transfer reaction pathway strongly depends on whether the *OOH intermediate exists or not, which makes this reaction pathway unclear for some cases. Anyway, considering all the situations, we conclude that C1′(SW-N3N3′) site is a good ORR active site. The use of materials with N-doped five-membered rings as precursors for CACs synthesis would enhance the concentration of N-doped SW-defect. The curvature effect of CACs can be realized by using CNTs or rippling graphene.[70] Moreover, the formation energy of a SW defect decreases significantly in CNTs compared with that in graphene. We hope that the present study may lead to improvement of the efficiency of PEMFC.

ASSOCIATED CONTENT

Supporting Information

The coordinates of G-N, G-NN(AB), SW-N3N3′, and SW-N2 structures for their corresponding graphene, the smallest and largest CNTs; equations for calculating the adsorption free energies of *O, *OH, and *OOH intermediates on CACs; derivation of eqs 6, 7, 9, and 13 in the main text; the treatment of spin states in the O_2 adsorption barrier calculations; example calculations for four different sites of the SW-N1 structure to support the correlation between the brightness of STM image and the O_2 adsorption barrier; derivation of the absolute adsorption Gibbs free energies of *O, *OH, and *OOH intermediates on CACs; curvature effects on the sp^2 to sp^3 conversion with the adsorption Gibbs free energy of *OH intermediate as an example; the details about the reaction pathways involving OH^- or OOH^- intermediate. This material is available free of charge via the Internet at http://pubs.acs.org.

AUTHOR INFORMATION

Corresponding Author

chai.g.aa@m.titech.ac.jp or guoliangchai@hotmail.com

Notes

The authors declare no competing financial interest.

■ ACKNOWLEDGMENTS

This work was performed under project no. 10000829-0 and project no. 10000832-0 at the New Energy and Industrial Technology Development Organization (NEDO). The computations were performed on TSUBAME Grid Cluster at the Global Scientific Information and Computing Center of Tokyo Institute of Technology. Parts of the computations were finished by using the supercomputing facilities in the Center for Information Science in JAIST.

■ REFERENCES

(1) Steele, B. C. H.; Heinzel, A. *Nature* **2001**, *414*, 345.
(2) Winter, M.; Brodd, R. J. *Chem. Rev.* **2004**, *104*, 4245.
(3) Yu, X. W.; Ye, S. Y. *J. Power Sources* **2007**, *172*, 145.
(4) Ozaki, J.; Nozawa, K.; Yamada, K.; Uchiyama, Y.; Yoshimoto, Y.; Furuichi, A.; Yokoyama, T.; Oya, A.; Brown, L. J.; Cashion, J. D. *J. Appl. Electrochem.* **2006**, *36*, 239LA.
(5) Gong, K. P.; Du, F.; Xia, Z. H.; Durstock, M.; Dai, L. M. *Science* **2009**, *323*, 760.
(6) Yang, D. S.; Bhattacharjya, D.; Inamdar, S.; Park, J.; Yu, J. S. *J. Am. Chem. Soc.* **2012**, *134*, 16127.
(7) Yang, Z.; Yao, Z.; Li, G. F.; Fang, G. Y.; Nie, H.; Liu, Z.; Zhou, X. M.; Chen, X.; Huang, S. M. *ACS Nano* **2011**, *6*, 205.
(8) Zhao, Y.; Yang, L. J.; Chen, S.; Wang, X. Z.; Ma, Y. W.; Wu, Q.; Jiang, Y. F.; Qian, W. J.; Hu, Z. *J. Am. Chem. Soc.* **2013**, *135*, 1201.
(9) Nallathambi, V.; Lee, J. W.; Kumaraguru, S. P.; Wu, G.; Popov, B. N. *J. Power Sources* **2008**, *183*, 34.
(10) Nabae, Y.; Sonoda, M.; Yamauchi, C.; Hosaka, Y.; Isoda, A.; Aoki, T. *Catal. Sci. Technol.* **2014**, *4*, 1400.
(11) Chokai, M.; Taniguchi, M.; Moriya, S.; Matsubayashi, K.; Shinoda, T.; Nabae, Y.; Kuroki, S.; Hayakawa, T.; Kakimoto, M.; Ozaki, J.; Miyata, S. *J. Power Sources* **2010**, *195*, 5947.
(12) Chen, Z.; Higgins, D.; Tao, H.; Hsu, R. S.; Chen, Z. W. *J. Phys. Chem. C* **2009**, *113*, 21008.
(13) Kundu, S.; Nagaiah, T. C.; Xia, W.; Wang, Y.; Dommele, S. V.; Bitter, J. H.; Santa, M.; Grundmeier, G.; Bron, M.; Schuhmann, W.; Muhler, M. *J. Phys. Chem. C* **2009**, *113*, 14302.
(14) Niwa, H.; Horiba, K.; Harada, Y.; Oshima, M.; Ikeda, T.; Terakura, K.; Ozaki, J.; Miyata, S. *J. Power Sources* **2009**, *187*, 93.
(15) Qu, L. T.; Liu, Y.; Baek, J. B.; Dai, L. M. *ACS Nano* **2010**, *4*, 1321.
(16) Yang, J. B.; Liu, D. J.; Kariuki, N. N.; Chen, L. X. *Chem. Commun.* **2008**, 329.
(17) Wang, X. L.; Hou, Z. F.; Ikeda, T.; Huang, S. F.; Terakura, K.; Boero, M.; Oshima, M.; Kakimoto, M.; Miyata, S. *Phys. Rev. B* **2011**, *84*, 245434.
(18) Wang, X. L.; Hou, Z. F.; Ikeda, T.; Oshima, M.; Kakimoto, M.; Terakura, K. *J. Phys. Chem. A* **2013**, *117*, 579.
(19) Hou, Z. F.; Wang, X. L.; Ikeda, T.; Terakura, K.; Oshima, M.; Kakimoto, M. *Phys. Rev. B* **2013**, *87*, 165401.
(20) Gao, F.; Zhao, G. L.; Yang, S. Z.; Spivey, J. J. *J. Am. Chem. Soc.* **2013**, *135*, 3315.
(21) Saidi, W. A. *J. Phys. Chem. Lett.* **2013**, *4*, 4160.
(22) Yu, L.; Pan, X. L.; Cao, X. M.; Hu, P.; Bao, X. H. *J. Catal.* **2011**, *282*, 183.
(23) Ni, S.; Li, Z. Y.; Yang, J. L. *Nanoscale* **2012**, *4*, 1184.
(24) Sidik, R. A.; Anderson, A. B.; Subramanian, N. P.; Kumaraguru, S. P.; Popov, B. N. *J. Phys. Chem. B* **2006**, *110*, 1787−1793.
(25) Kurak, K. A.; Anderson, A. B. *J. Phys. Chem. C* **2009**, *113*, 6730.
(26) Kim, H.; Lee, K.; Woo, S. I.; Jung, Y. *Phys. Chem. Chem. Phys.* **2011**, *13*, 17505.
(27) Li, Q.; Zhang, S.; Dai, L.; Li, L.-s. *J. Am. Chem. Soc.* **2012**, *134*, 18932.
(28) Li, Q.; Noffke, B. W.; Wang, Y.; Menezes, B.; Peters, D. G.; Raghavachari, K.; Li, L. S. *J. Am. Chem. Soc.* **2014**, *136*, 3358.
(29) McClure, J. P.; Thornton, J. D.; Jiang, R.; Chu, D.; Cuomo, J. J.; Fedkiw, P. S. *J. Electrochem. Soc.* **2012**, *159*, F733.
(30) Wu, G.; More, K. L.; Johnston, C. M.; Zelenay, P. *Science* **2011**, *332*, 443.
(31) Ikeda, T.; Boero, M.; Huang, S. F.; Terakura, K.; Oshima, M.; Ozaki, J. *J. Phys. Chem. C* **2008**, *112*, 14706.
(32) Ikeda, T.; Hou, Z. F.; Chai, G. L.; Terakura, K. *J. Phys. Chem. C* **2014**, *118*, 17616.
(33) Huang, S. F.; Terakura, K.; Ozaki, T.; Ikeda, T.; Boero, M.; Oshima, M.; Ozaki, J.; Miyata, S. *Phys. Rev. B* **2009**, *80*, 235410.
(34) Hou, Z. F.; Wang, X. L.; Ikeda, T.; Terakura, K.; Oshima, M.; Kakimoto, M.; Miyata, S. *Phys. Rev. B* **2012**, *85*, 165439.
(35) Chokai, M.; Nabae, Y.; Kuroki, S.; Hayakawa, T.; Kakimoto, M.; Miyata, S. *J. Photopolym. Sci. Technol.* **2011**, *24*, 241.
(36) Lee, Y. H.; Li, F.; Chang, K. H.; Hu, C. C.; Ohsaka, T. *Appl. Catal., B* **2012**, *126*, 208.
(37) Shan, B.; Cho, K. *Chem. Phys. Lett.* **2010**, *492*, 131.
(38) Nørskov, J. K.; Rossmeisl, J.; Logadottir, A.; Lindqvist, L.; Kitchin, J. R.; Bligaard, T.; Jónsson, H. *J. Phys. Chem. B* **2004**, *108*, 17886.
(39) Anderson, A. B. *Phys. Chem. Chem. Phys.* **2012**, *14*, 1330.
(40) Calle-Vallejo, F.; Martinez, J. I.; Rossmeisl, J. *Phys. Chem. Chem. Phys.* **2011**, *13*, 15639.
(41) Greeley, J.; Stephens, I. E. L.; Bondarenko, A. S.; Johansson, T. P.; Hansen, H. A.; Jaramillo, T. F.; Rossmeisl, J.; Chorkendorff, I.; Nørskov, J. K. *Nature Chem.* **2009**, *1*, 552.
(42) Car, R.; Parrinello, M. *Phys. Rev. Lett.* **1985**, *55*, 2471.
(43) *CPMD*; IBMCorp., 1990−2006; http://www.cpmd.org.
(44) Sprik, M.; Ciccotti, G. *J. Chem. Phys.* **1998**, *109*, 7737.
(45) Troullier, N.; Martins, J. L. *Phys. Rev. B* **1991**, *43*, 1993.
(46) Sprik, M.; Hutter, J.; Parrinello, M. *J. Chem. Phys.* **1996**, *105*, 1142.
(47) Hamprecht, F. A.; Cohen, A. J.; Tozer, D. J.; Handy, N. C. *J. Chem. Phys.* **1998**, *109*, 6264.
(48) It is known that LDA and GGA give poor results for the binding energy E_b and bond distance d of the O_2 molecule in the triplet state. For example, LDA gives d = 1.22 Å and E_b = 7.2 eV, while GGA-PBE gives d = 1.23 Å and E_b = 5.68 eV. Giannozzi, P.; Car, R.; Scoles, G. *J. Chem. Phys.* **2003**, *118*, 1003. On the other hand, GGA-HTCH gives d = 1.225 Å and E_b = 5.04 eV, which are in good agreement with the experimental values of d = 1.207 Å and E_b = 5.12 eV.
(49) Giannozzi, P.; Baroni, S.; Bonini, N.; Calandra, M.; Car, R.; Cavazzoni, C.; Ceresoli, D.; Chiarotti, G. L.; Cococcioni, M.; Dabo, I.; Corso, A. D.; Gironcoli, S.; Fabris, S.; Fratesi, G.; Ralph, G.; Gerstmann, U.; Gougoussis, C.; Kokalj, A.; Lazzeri, M.; Martin-Samos, L.; Marzari, N.; Mauri, F.; Mazzarello, R.; Paolini, S.; Pasquarello, A.; Paulatto, L.; Sbraccia, C.; Scandolo, S.; Sclauzero, G.; Seitsonen, A. P.; Smogunov, A.; Umari, P.; Wentzcovitch, R. M. *J. Phys.: Condens. Matter.* **2009**, *21*, 395502.
(50) Perdew, J. P.; Burke, K.; Ernzerhof, M. *Phys. Rev. Lett.* **1996**, *77*, 3865.
(51) Rossmeisl, J.; Logadottir, A.; Nørskov, J. K. *Chem. Phys.* **2005**, *319*, 178.
(52) Fukui, K.; Yonezawa, T.; Shingu, H. *J. Chem. Phys.* **1952**, *20*, 722.
(53) Fukui, K. *Science* **1982**, *218*, 747.
(54) Woodward, R. B.; Hoffmann, R. *Angew. Chem., Int. Ed.* **1969**, *8*, 781.
(55) Viswanathan, V.; Hansen, H. A.; Rossmeisl, J.; Nørskov, J. K. *J. Phys. Chem. Lett.* **2012**, *3*, 2948.
(56) Anderson, A. B.; Jinnouchi, R.; Uddin, J. *J. Phys. Chem. C* **2013**, *117*, 41.
(57) Nørskov's method uses H_2O and H_2 as references to avoid the treatment of the triplet O_2 molecule. This is reasonable because the ordinary GGA-PBE functional cannot treat triplet O_2 molecule accurately while it has no problem treating the adsorbed structures of the intermediates. However, these references make the calculated adsorption Gibbs free energy for the intermediates *OOH, *OH, and *O positive even for strong bonded structures. In this paper, we calculate all the adsorption Gibbs free energy and derive the equations by following Nørskov's method. However, we also convert the adsorption Gibbs free energy calculated by Nørskov's method to the absolute adsorption Gibbs free energy for the intermediates. These absolute adsorption Gibbs free energies can represent the true bond

strength for the adsorption of *O, *OH, and *OOH intermediates on the substrates.
(58) Man, I. C.; Su, H. Y.; Calle-Vallejo, F.; Hansen, H. A.; Martnez, J. I.; Inoglu, N. G.; Kitchin, J.; Jaramillo, T. F.; Nørskov, J. K.; Rossmeisl, J. *ChemCatChem* **2011**, *3*, 1159.
(59) Sabatier, P. *Ber. Dtsch. Chem. Ges.* **1911**, *44*, 1984.
(60) Haneman, D. *Phys. Rev.* **1961**, *121*, 1093.
(61) Hashimoto, T.; Morikawa, Y.; Fujikawa, Y.; Sakurai, T.; Lagally, M. G.; Terakura, K. *Surf. Sci.* **2002**, *513*, L445.
(62) Tripković, V.; Skúlason, E.; Siahrostami, S.; Nørskov, J. K.; Rossmeisl, J. *Electrochim. Acta* **2010**, *55*, 7975.
(63) Saidi, W. A. *J. Phys. Chem. A* **2013**, *118*, 7235.
(64) Vinten, P.; Marshall, P.; Lefebvre, J.; Finnie, P. *J. Phys. Chem. C* **2013**, *117*, 3527.
(65) Okamoto, Y. *Appl. Surf. Sci.* **2009**, *256*, 335.
(66) Gileadi, E. *J. Electroanal. Chem.* **2002**, *532*, 181.
(67) Aguirre-Soto, A.; Lim, C.-H.; Hwang, A. T.; Musgrave, C. B.; Stansbury, J. W. *J. Am. Chem. Soc.* **2014**, *136*, 7418.
(68) Moore, J. W.; Stanitsuki, C. L.; Jurs, P. C. *Chemistry: The Molecular Science*, 4th ed.; Brooks/Cole: Singapore, 2011; Appendix J.
(69) In our FPMD simulation for SW-N3N3′, *OOH persists for about 8 ps and then decomposes into *O and OH^-(aq). Note, however, that the use of a rather small unit cell may impede additional electron transfer from the substrate to the adduct. If the unit cell becomes much larger, the electron transfer may become easier and the lifetime of *OOH may become shorter.
(70) Shenoy, V. B.; Reddy, C. D.; Ramasubramaniam, A.; Zhang, Y. W. *Phys. Rev. Lett.* **2008**, *101*, 245501.